CrossMark

MPCE

Predictive control of plug-in electric vehicle chargers with photovoltaic integration

Adrian Soon Theam TAN[1] , Dahaman ISHAK[1], Rosmiwati MOHD-MOKHTAR[1],
Sze Sing LEE[2], Nik Rumzi Nik IDRIS[3]

Abstract This paper presents a model predictive control (MPC) for off-board plug-in electric vehicle (PEV) chargers with photovoltaic (PV) integration using two-level four-leg inverter topology. The PEV charger is controlled by a unified controller that incorporates direct power and current MPC to dynamically control decoupled active-reactive power flow in a smart grid environment as well as to control PEV battery charging and discharging reliably. PV power generation with maximum power tracking is seamlessly integrated with the power flow control to provide additional power generation. Fast dynamic response and good steady-state performance under all power flow modes and various environmental conditions are evaluated and analyzed. From the results obtained, the charger demonstrates less than 1.5% total harmonic distortion as well as low active and reactive power ripple of less than 7% and 8% respectively on the grid for all power flow modes. The PEV battery also experiences a low charging and discharging current ripple of less than 2.5%. Therefore, the results indicate the successful implementation of the proposed charger and its control for PV integrated off-board PEV chargers.

Keywords Plug-in electric vehicles, Electric vehicle charger, Photovoltaic generation, Model predictive control

1 Introduction

As the adoption of plug-in electric vehicles (PEVs) continue to increase, the power grid experiences new challenges in terms of grid stability, reliability, power quality and harmonics [1–6]. This has led to extensive research on bidirectional PEV chargers that feature grid-to-vehicle (G2V) operations for battery charging as well as vehicle-to-grid (V2G) operations. V2G operations of bidirectional PEV chargers are highly attractive due to the potential of PEVs fulfilling the energy storage needs of the grid and assisting the grid in terms of providing active power for load leveling, reactive power support, ancillary services, voltage regulation, harmonic filtering and power factor correction [7–14]. Supplying reactive power using on-board chargers that are connected to a distribution system has some inherent disadvantages, such as the mobility and the power limitation of on-board chargers [15, 16]. V2G services using off-board chargers are more advantageous compared with using on-board chargers since off-board stations are stationary and are rated at higher

✉ Adrian Soon Theam TAN
  adriantst90@hotmail.com

  Dahaman ISHAK
  dahaman@usm.my

  Rosmiwati MOHD-MOKHTAR
  eerosmiwati@usm.my

  Sze Sing LEE
  ss.lee@soton.ac.uk

  Nik Rumzi Nik IDRIS
  nikrumzi@fke.utm.my

[1] School of Electrical and Electronic Engineering, Universiti Sains Malaysia, 14300 Nibong Tebal, Penang, Malaysia

[2] University of Southampton Malaysia Campus, Nusajaya, Johor, Malaysia

[3] UTM-PROTON Future Drive Laboratory, Universiti Teknologi Malaysia, 81310 Skudai, Johor, Malaysia

STATE GRID
STATE GRID ELECTRIC POWER RESEARCH INSTITUTE

power levels. Hence, the utility grid can compensate respective stations via an annual agreement [15].

Furthermore, charging stations can be integrated with renewable energy sources (RES) such as wind or solar with suitable maximum power point trackers to lessen grid dependency. PEVs can act as distributed energy storage units attribute to the large energy reserve of an electric vehicle battery and the potential of thousands of units connected to the grid. Hence, by integrating RES with charging stations, the impact of PEV charging on the electric grid can be mitigated, while at the same time helping to achieve renewable portfolio standards [17–24].

To provide reactive power compensation without degrading PEV's battery during charging, several research works on bidirectional PEV chargers have been reported. A bidirectional off-board charger proposed by [15] employs two linear controllers to track reference active power and reactive power in conjunction with a phase-locked loop algorithm. The proposed charger is capable of four quadrant operations but does not have RES integration, thus limiting its potential to be self-sufficient. Meanwhile, in a single-phase on-board bidirectional charger proposed by [25], proportional-integral (PI) controllers are employed in AC/DC converters and DC/DC converters to provide constant voltage and constant current charging as well as reactive power compensation. However, the proposed charger is only capable for two quadrants of operation. Reference [26] proposes a PEV DC charging station using a neutral point clamped converter. The proposed DC bus architecture allows the connection of distributed power systems such as RES and energy storage devices. The grid-connected converter in the system is regulated using voltage oriented control with multiple linear controllers and for the voltage balancing mechanism, another linear control is utilized. In a separate study, a unified single-phase and three-phase control of on-board PEV chargers proposed by [27] utilizes separate linear controllers with respective references to provide desired control for grid power flow and battery charging.

In the aforementioned PEV chargers [15, 25–27], their control of desired variables as well as the modulation required to generate the expected voltage are realized using linear controllers such as PI controllers. In order to fulfill numerous control requirements, the linear controllers are cascaded with multiple outer loops that may result in higher bandwidth for the inner controller loops. Although this control technique is easy to implement, its performance for the whole system is heavily dependent on the performance of the inner control loop. For this reason, the parameters of the inner controller must be chosen carefully to provide system stability at all operating points.

Moreover, the usage of linear controllers leads to more complicated and time consuming gain tuning [28–30].

In recent years, finite control set model predictive control (FCS-MPC) has gained greater popularity due to having several advantages such as fast dynamic response, easy inclusion of nonlinearities and constraints of the system and the flexibility to include other system requirements in the controller [31–33]. FCS-MPC is an optimization problem where a sequence of future actuations is obtained by minimizing the cost function. Since power converters are systems with finite number of states, the MPC optimization problem can be simplified and reduced to the prediction of the behavior of the system for each possible state. Extensive research work has been done on performance evaluation between FCS-MPC and traditional linear-based controllers such as the PI controller [31, 34–41].

In terms of dynamic response, FCS-MPC is slightly faster and has less overshoot than the PI controller. Furthermore, the PI controller suffers from decoupling capability between the d and q axes. From the studies in [31, 37, 41], the current in the q axis is disturbed when step changes in the d axis current reference are applied. This coupling is not present in the response of the FCS-MPC. In addition, FCS-MPC requires simpler implementation as compared to linear controllers, since saturation of the manipulated variables, anti-windup protection, decoupling networks, modulator and tuning of the controller parameters are not required. In addition, numerous research studies have established that FCS-MPC yields smaller total harmonic distortion (THD) and smaller mean absolute current reference tracking error as compared to traditional linear controllers [31, 36, 37, 40, 41]. Hence, FCS-MPC could be an excellent alternative for PEV charger control. However, there is a lack of application of MPC using either current control or power control in the PEV charger. To the author's best knowledge, the MPC of the PEV charger with renewable energy integration has never been reported.

Motivated to fill this research gap, this paper presents a model predictive control (MPC) of off-board PEV chargers with photovoltaic (PV) integration using two-level four-leg inverter topology. The charger operates in four quadrants in the active-reactive power planes to achieve multiple functions (i.e. PEV battery charging, PEV battery discharging for load leveling, providing reactive power support and acquiring maximum PV power generation). The control of the four quadrant modes is realized by incorporating both direct power and current MPC that dynamically controls the decoupled active-reactive power flow in a smart grid environment as well as controlling the PEV battery charging and discharging reliably.

Through implementation of direct power and current MPC, optimal switching states for the charger is directly

generated, thus eliminating the need for a modulator. By adopting direct power and direct current FCS-MPC, the charger is able to provide higher quality of power and current with low THD and ripple content for the grid's power flow and PEV charging as well as good dynamic response to the overall system. In addition, using the proposed control strategy, PV generation with maximum power tracking could be seamlessly integrated with the power flow control to provide additional power generation to charge the PEV battery or supplied to the grid, reducing the grid dependency on the charging station. Detailed analyses of the proposed system and its control are presented here. The results show that the charger exhibits fast dynamic response and good steady-state performance under all power flow modes and various environmental conditions. The remainder of the paper is arranged as follows. Section 2 elaborates on the proposed system topology and control algorithm. Section 3 presents the simulation study of the proposed system and its performance analysis. Finally, a conclusion is drawn in Section 4.

2 PEV chargers with PV integration

2.1 System configuration

Figure 1 shows the circuit configuration of the proposed PEV charger system with PV integration. The system consists of two integral stages, AC/DC converter and DC/DC converter. The AC/DC converter is a three-phase voltage source converter (VSC). The VSC is responsible for directing the power flow of the system by controlling switches S_1 to S_6 with the help of model predictive direct power control (MPDPC). Active power can be drawn from the grid for PEV battery charging as well as additional power generated by the PV array can be fed back to the grid seamlessly. At the same time, reactive power support can be delivered to the grid when requested by the utility using MPDPC.

Hence, the proposed PEV charger system operates in all four quadrants of the power plane as illustrated in Fig. 2. In the meantime, the DC/DC converter controls the PEV
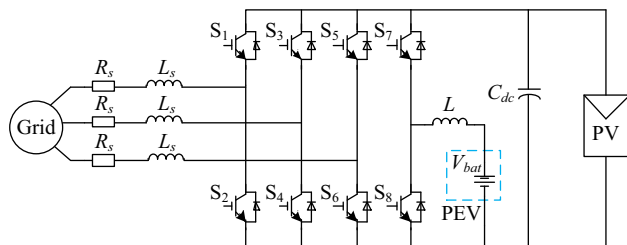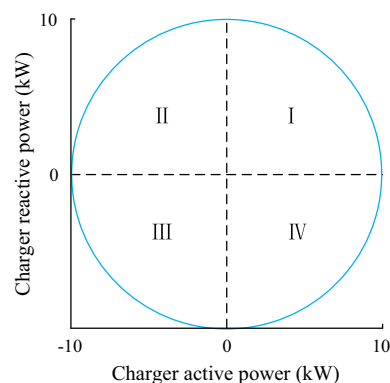
Fig. 2 Power flow operation of PEV charger

battery charging through switches S_7 and S_8. A current MPC is implemented to control battery's charging and discharging. When S_7 is turned on and S_8 is turned off, the current flows through S_7 and the inductor L, thus charging the battery. When S_7 is turned off, the free-wheeling diode of switch S_8 conducts the inductor current back to the inductor and battery. During this operation, the voltage at the DC link is stepped down from 400-600 V to 240 V.

Hence, buck converter operation is achieved during battery charging. Meanwhile, when S_8 is turned on and S_7 is turned off, the battery current energizes the inductor. When S_8 is turned off, the inductor current flows through the free-wheeling diode of switch S_7, thus sending power back into the grid. During this boost operation, the battery voltage of 240 V is stepped up to the 400-600 V range. Note that active power and reactive power sent from the grid to the charger have a positive sign and vice versa. While a negative sign for the battery's power denotes that the battery is receiving power from the grid and vice versa. These notations will be used throughout this paper. A detailed description of applied MPC can be found in the next section.

2.2 Predictive control of bidirectional power flow between AC and DC terminals

Figure 3 shows the control diagram of the MPC of the proposed PEV charger system. From the diagram, there are two predictive models in charge of providing the optimal switching action to switches S_1 to S_8 of the proposed charger. The proposed predictive strategy is based on the fact that only a finite number of possible switching states are available to the power converter.

The first predictive model is responsible for controlling the switching of the VSC (switches S_1 to S_6) to control active and reactive power flow between the AC and DC terminals as well as controlling the DC link voltage. First, the grid phase voltages and phase currents are sampled in
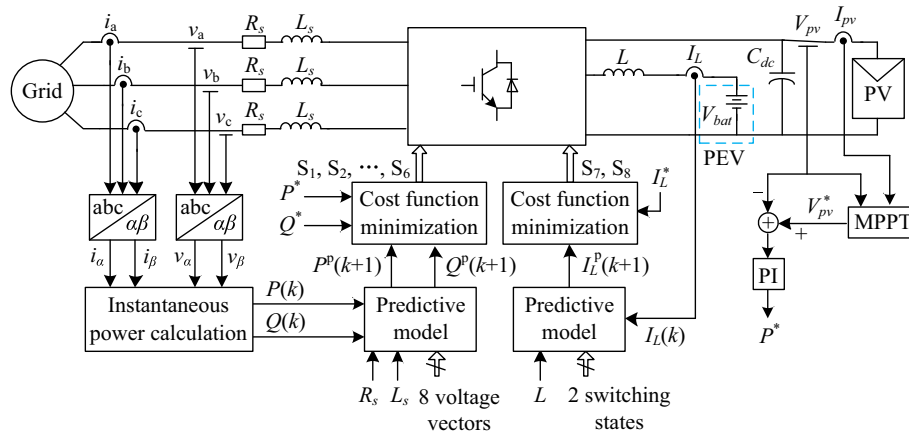
Fig. 1 Configuration of the proposed PEV charger system

Fig. 3 Control diagram of MPC of PEV charger system

order to calculate the grid's instantaneous power for the predictive model. Since the upper and lower switches of the VSC are operating in a complementary mode, there are eight different switching states available, which lead to the formulation of seven different voltage vectors in the $\alpha\beta$ orthogonal coordinates, as illustrated in Fig. 4.

There are a total of six active vectors and two zero vectors. Voltage vectors generated by the inverter, when expressed in terms of switching states and DC link voltage are:

$$v_{\alpha\beta} = \sqrt{\frac{2}{3}}V_{dc}\left(S_a + S_b e^{j\frac{2\pi}{3}} + S_c e^{j\frac{4\pi}{3}}\right) \tag{1}$$

where S_a, S_b and S_c are the switching states at each leg of the inverter. The switching states can be represented in binary states 1 or 0 at which state 1 indicates that the upper switch is on and the lower switch is off and vice versa for binary state 0. Hence, the voltage vectors are represented in the form of $(S_a S_b S_c)$ as shown in Fig. 4.

In order to produce instantaneous active and reactive power for the predictive controller, the grid voltages and
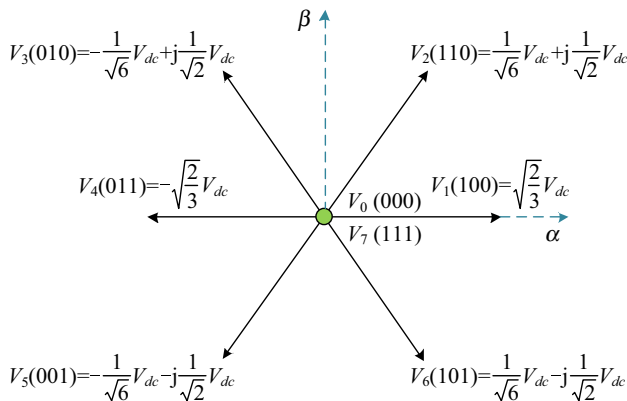
currents are first measured. Then, the grid voltages and currents are expressed in a stationary reference $\alpha\beta$ frame by using power invariant Clarke transformation, which is given by:

$$\begin{bmatrix} v_\alpha \\ v_\beta \end{bmatrix} = \sqrt{\frac{2}{3}}\begin{bmatrix} 1 & -\frac{1}{2} & -\frac{1}{2} \\ 0 & \frac{\sqrt{3}}{2} & -\frac{\sqrt{3}}{2} \end{bmatrix}\begin{bmatrix} v_a \\ v_b \\ v_c \end{bmatrix} \tag{2}$$

$$\begin{bmatrix} i_\alpha \\ i_\beta \end{bmatrix} = \sqrt{\frac{2}{3}}\begin{bmatrix} 1 & -\frac{1}{2} & -\frac{1}{2} \\ 0 & \frac{\sqrt{3}}{2} & -\frac{\sqrt{3}}{2} \end{bmatrix}\begin{bmatrix} i_a \\ i_b \\ i_c \end{bmatrix} \tag{3}$$

The three-phase VSC is connected to the grid through an inductor with an inductance of L_s and an equivalent series resistance (ESR) of R_s. Although the ESR of the inductor is small and can be neglected, it is taken into consideration here for more precise control of the power. By applying Kirchoff's voltage law at the VSC, the grid voltage, $v_{s\alpha\beta}$ can be expressed as:

$$v_{s\alpha\beta} = L_s\frac{di_{\alpha\beta}}{dt} + R_s i_{\alpha\beta} + v_{o\alpha\beta} \tag{4}$$

where $i_{\alpha\beta}$ denotes the grid current; $v_{o\alpha\beta}$ denotes the output voltage of the converter, all in the $\alpha\beta$ reference frame. Thus, the derivative of the phase current components can be obtained as:

$$\frac{di_\alpha}{dt} = \frac{1}{L}\left(v_{s\alpha} - v_{o\alpha} - i_\alpha R_s\right) \tag{5}$$

$$\frac{di_\beta}{dt} = \frac{1}{L}\left(v_{s\beta} - v_{o\beta} - i_\beta R_s\right) \tag{6}$$

The power invariant instantaneous active and reactive power are given by:

$$P = v_{s\alpha}i_\alpha + v_{s\beta}i_\beta \tag{7}$$

Fig. 4 Voltage vectors for VSC

$$Q = v_{s\beta}i_\alpha - v_{s\alpha}i_\beta \tag{8}$$

Then, differentiating (6) and (7) yields:

$$\frac{dP}{dt} = v_{s\alpha}\frac{di_\alpha}{dt} + i_\alpha\frac{dv_{s\alpha}}{dt} + v_{s\beta}\frac{di_\beta}{dt} + i_\beta\frac{dv_{s\beta}}{dt} \tag{9}$$

$$\frac{dQ}{dt} = v_{s\beta}\frac{di_\alpha}{dt} + i_\alpha\frac{dv_{s\beta}}{dt} - v_{s\alpha}\frac{di_\beta}{dt} - i_\beta\frac{dv_{s\alpha}}{dt} \tag{10}$$

By considering the balanced sinusoidal three-phase voltages at grid frequency ω_s (rad/s) in the system, the grid voltages can be denoted as:

$$v_{s\alpha} = v_s \sin(\omega_s t) \tag{11}$$

$$v_{s\beta} = -v_s \cos(\omega_s t) \tag{12}$$

Subsequently, the derivative of the grid voltages can be obtained as:

$$\frac{dv_{s\alpha}}{dt} = -\omega_s v_{s\beta} \tag{13}$$

$$\frac{dv_{s\beta}}{dt} = \omega_s v_{s\alpha} \tag{14}$$

By substituting (11) to (14) into (9) and (10), and simplifying with (7) and (8), the resulting dynamic models of the active and reactive power are:

$$\frac{dP}{dt} = \frac{1}{L}(v_{s\alpha}^2 + v_{s\beta}^2 - v_{s\alpha}v_{o\alpha} - v_{s\beta}v_{o\beta} - R_sP) - \omega_sQ \tag{15}$$

$$\frac{dQ}{dt} = \frac{1}{L}(v_{s\alpha}v_{o\beta} - v_{s\beta}v_{o\alpha} - R_sQ) + \omega_sP \tag{16}$$

Considering the power variation within one switching period T_s, discretization of (10) enables the calculation of the predicted active and reactive power at the next sampling instant $P^p(k+1)$ and $Q^p(k+1)$, i.e.,

$$P^p(k+1) = P(k) + \frac{T_s}{L}\left(v_{s\alpha}^2(k) + v_{s\beta}^2(k) - v_{s\alpha}(k)v_{o\alpha}(k) \right.$$
$$\left. - v_{s\beta}(k)v_{o\beta}(k) - R_sP(k)\right) - \omega_sT_sQ(k) \tag{17}$$

$$Q^p(k+1) = Q(k) + \frac{T_s}{L}\left(v_{s\alpha}(k)v_{o\beta}(k) - v_{s\beta}(k)v_{o\alpha}(k) \right.$$
$$\left. - R_sQ(k)\right) + \omega_sT_sP(k) \tag{18}$$

Following the principle of MPC, a quadratic cost function which computes the deviation between the reference power and predicted power is minimized by selecting the optimal voltage vector from all of the possible candidate voltage vectors as illustrated in Fig. 4. The cost function g_1 is represented as:

$$g_1 = (P^* - P^p(k+1))^2 + (Q^* - Q^p(k+1))^2 \tag{19}$$

where P^* denotes the reference active power and Q^* denotes the reference reactive power. $P^p(k+1)$ and $Q^p(k+1)$ are calculated by using (17) and (18) respectively for each of the seven possible voltage vectors shown in Fig. 4. Then, the cost function g_1 evaluates the error between the reference and predicted active power and reactive power in the next sampling interval. The voltage that minimizes the cost function g_1 and has the smallest error is selected as the optimal voltage vector and is then applied to the system.

2.3 Predictive control of PEV for charging and discharging operations

Meanwhile, the second predictive model in Fig. 3 is responsible for regulating the charging and discharging of the PEV battery by controlling switches S_7 and S_8. A reference battery power, P^*_{bat} is delivered to the predictive controller to determine the operation of the DC/DC converter. By setting the battery charging voltage to a predetermined level (240 V), the control of the power flow for the battery could be simplified and achieved with a single current predictive control to control inductor current I_L. The inductor current, I_L is first sampled and its value is used to predict the inductor current in the next sampling period. Then, the inductor voltage, V_L can be represented as:

$$V_L = L\frac{dI_L}{dt} \tag{20}$$

In order to obtain the predicted inductor current at the next sampling instant, (20) is discretized and rearranged, yielding:

$$\begin{cases} V_L = L\dfrac{I_L^p(k+1) - I_L(k)}{T_s} \\ I_L^p(k+1) = \dfrac{T_s}{L}V_L + I_L(k) \end{cases} \tag{21}$$

Since there are only two switches involved in the current predictive control (S_7 and S_8) and they are working in complementary mode, there are only two possible voltage vectors available.

When S_7 is turned off and S_8 is turned on, V_L is equal to the battery's voltage V_{bat}. Conversely, when S_7 is turned on and S_8 is turned off, V_L is equal to $V_{bat} - V_{pv}$ where V_{pv} is the PV array's voltage. Then, the cost function, g_2 evaluates the error between the predicted inductor current and the sampled inductor. Cost function g_2 can be represented as:

$$g_2 = (I_L^* - I_L^p(k+1))^2 \tag{22}$$

Finally, the voltage vector that yields the lesser error is implemented for the current control.

2.4 Maximum power point tracking of PV array

On the PV array side, a maximum power point tracking (MPPT) using perturb and observe algorithms is implemented to extract maximum available PV power to feed into the system. The MPPT algorithm will produce a reference voltage point V_{pv}^*. The difference between the voltage reference and DC link capacitor voltage will then be inserted into a PI controller in order to compute the reference active power for cost function g_1. It is important to note that the range of PV array's voltage which corresponds to the maximum power point, V_{MPP} must be within the range of the DC link capacitor voltage. If the V_{MPP} is located beyond the range of the DC link capacitor voltage, an additional buck or boost converter is needed to step-up or step-down the PV array's voltage to the appropriate voltage level in the DC link capacitor.

2.5 Summary of the control algorithm

The control algorithm is comprised of two MPCs to handle the bidirectional power flow between the AC and DC terminals and the control of the PEV charging and discharging. Cost function minimization is implemented as a repeated loop for each voltage vector to predict the active power, reactive power, and inductor current values, evaluate the cost function, and store the minimum value and the index value of the corresponding switching state for the respective switches.

The control of the bidirectional power flow can be summarized as follows:

1) Sample the input phase current i_{abc} and input phase voltage v_{abc}.
2) Express those phase currents and voltages in stationary reference $\alpha\beta$ frame by using the power invariant Clarke transformation.
3) Those values are used to predict the active power and reactive power by using (17) and (18).
4) All predictions are evaluated by using the cost function g_1.
5) The optimal switching state that corresponds to the optimal voltage vector that minimizes the cost function is selected to be applied at the next sampling time.

Meanwhile, the control of PEV charging and discharging can be summarized as follows:

1) Sample inductor current I_L.
2) The sampled value is used to predict the inductor current by using (21).
3) All predictions are evaluated using the cost function g_2.

4) The optimal switching state that minimizes the cost function is selected to be applied at the next sampling time.

3 Simulation results

In order to evaluate the performance of the proposed PEV charger system, the system is implemented in the MATLAB/Simulink environment. The system parameters are listed in Table 1.

3.1 Power flow modes

The proposed system has multiple power flow modes depending on various system parameters such as the amount of PV power generated, reactive power demand, and the power level of the PEV battery. Therefore, the system is simulated for all possible power flow modes in order to evaluate its effectiveness and performance. For an exhaustive study, the system is simulated at its maximum operating range, i.e. ±10 kW battery active power, ±10 kvar grid reactive power and 12.5 kW to 0 kW PV power. Table 2 illustrates the various modes of power flow of the proposed system and Fig. 5 presents the corresponding simulation results. In order to operate the PEV charger in a single mode, the active power of the PEV battery, PV power generation and the grid's reactive power are set according to the parameters in Table 2.

From Fig. 5, the simulation starts with mode "000" and ends with mode "111" and each mode transition is set to occur every 5 s in the simulation. Mode "000" represents that the PEV battery receives 10 kW of active power from the grid for charging, the PV array does not provide any active power generation while the grid receives 10 kvar of reactive power. Similarly for mode "111", the PEV battery supplies 10 kW of active power to the grid, the PV array is generating 12.5 kW of active power while the grid supplies 10 kvar of reactive power. In these modes, the switches will operate based on the MPC implemented in the system that yields the smallest cost function.

The DC link capacitor voltage which corresponds to the voltage of the PV array, V_{pv} is determined by the MPPT algorithm which extracts the maximum available PV power. As can be seen from Fig. 5, the range of V_{pv} is limited to within 400 V to 600 V.

Depending on the state of the PEV battery, the grid supplies and receives active power accordingly. During the first half of the simulation (mode "000" to "011"), the PEV battery receives 10 kW of active power for charging. Since the PV array initially does not provide any power (modes "000" and "001"), the grid supplies 10 kW of

Table 1 System parameters used in the proposed system

Parameter	Symbol	Value
Charger apparent power	S	14.1 kVA
Root mean square (RMS) of three-phase line-to-line grid voltage	V_{ab}	208 V
Line inductance	L_s	5 mH
Line resistance	R_s	0.03 Ω
Grid frequency	f	50 Hz
Battery voltage	V_{bat}	240 V
Boost inductor	L	11 mH
DC link capacitor	C_{dc}	1000 μF

Table 2 Various modes of power flow of the proposed system

Mode	P_{bat} (kW)	P_{pv} (kW)	Q (kvar)
000	− 10	0	− 10
001	− 10	0	10
010	− 10	12.5	− 10
011	− 10	12.5	10
100	10	0	− 10
101	10	0	10
110	10	12.5	− 10
111	10	12.5	10

active power to the battery. Then, the PV array starts to supply 12.5 kW of power (modes "010" and "011") and the battery receives the 10 kW of active power required for charging while the grid absorbs the remaining excess power from the PV array. Note that from the figure, the active power of the grid falls from the positive region to negative region at mode "011" signifying that the grid is receiving net active power. During the second half of the simulation, the PEV battery supplies active power to the grid for the V2G operation and the active power of the grid further falls deeper into the negative region, signifying that the grid receives even more active energy. Throughout the simulation as shown in Fig. 5, the converter is also able to supply and receive reactive power without affecting the various active power transfers within the system.

In a separate simulation to study the active power flow in the system, the reactive power reference is set to zero while the battery reference power is set to − 10 kW. Figure 6 shows the grid voltage and current for phase a when PV power generation is turned on. Initially, the grid is supplying 10 kW of active power to the PEV battery for charging without PV power generation and the grid voltage is in phase with its grid current.

Once PV generation is activated at $t = 0.1$ s, the MPPT algorithm begins to track the maximum available power and the PV array starts to supply active power to the

charger. During this event, the magnitude of the grid current gradually decreases, as shown in the figure, indicating that the grid is reducing active power to the battery. After approximately 0.2 s, the grid current is almost zero, hence negligible power transfer occurs from the grid. This shows that the net power flow from the PV array is equal to the power received by the PEV battery for charging. Shortly after, there is a 180 degrees phase change in the grid current with respect to the grid voltage signifying that the direction of the power flow is reversed. At this moment, the maximum point of the PV array is reached and the PV array generates 12.5 kW of active power into the charger. Therefore, the proposed charger supplies 10 kW of active power from the PV array to the PEV battery for charging and forwards the remaining 2.5 kW of active power back to the grid. Hence, the proposed charger is successfully proven to be able to efficiently control the power flow from various sources.

3.2 PV MPPT performance under various temperatures and irradiances

A perturb and observe MPPT algorithm is implemented in the system to extract maximum availability of the PV power from the PV array under various environmental conditions. Two important factors that affect the location of the maximum power point of the PV array are the incident irradiance and the operating temperature of the array. Therefore, a simulation study is conducted with different irradiances and temperatures to investigate the effectiveness of the algorithm in tracking the maximum power.
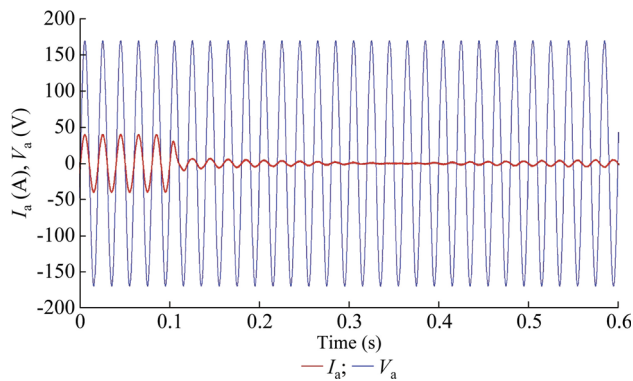
Figure 7 shows the PV MPPT performance of the proposed PEV system under the aforementioned testing conditions.

In this simulation study, P_{bat} is set to − 10 kW to receive power for battery charging while the charger is set to consume 10 kvar excess reactive power from the grid. From Fig. 7, it can be pointed out that V_{MPP} is located
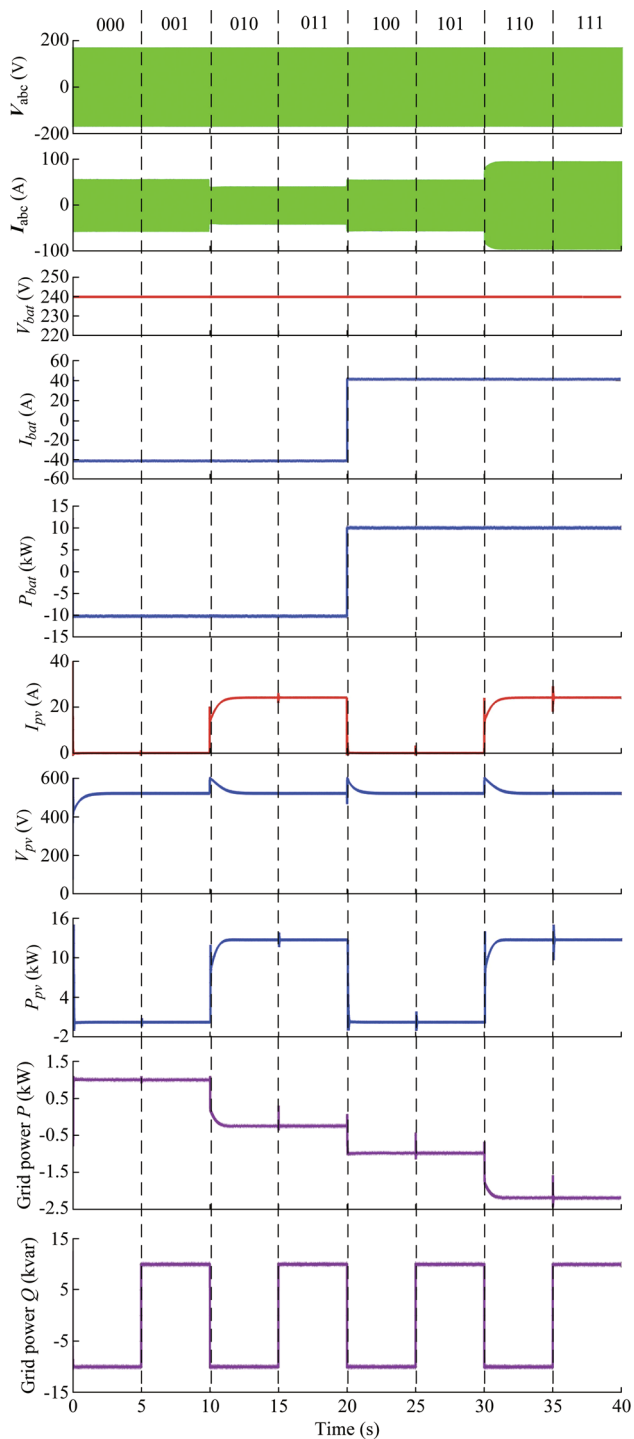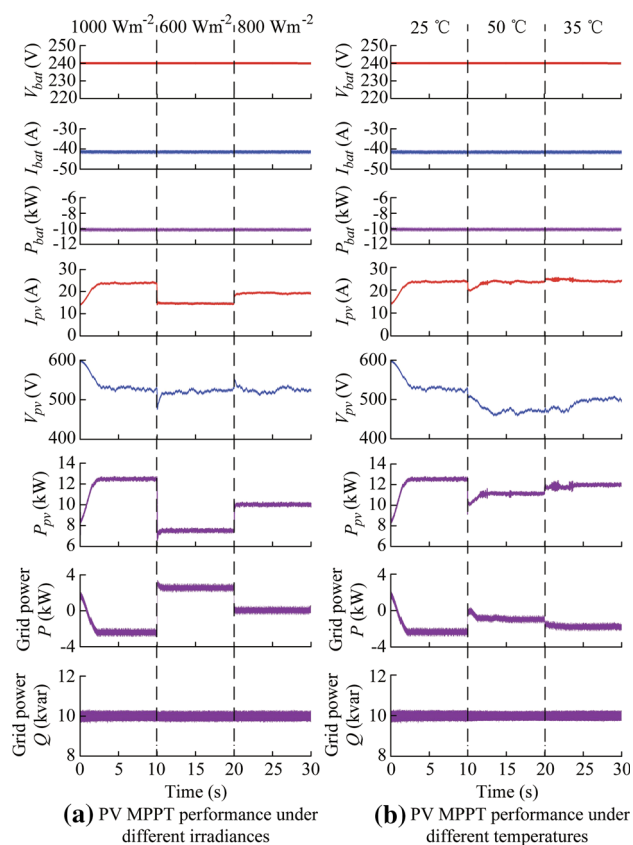
Fig. 5 Simulation results of various power flow modes of the proposed PEV system

Fig. 6 Grid voltage and current for phase a when PV power generation is turned on

(a) PV MPPT performance under different irradiances

(b) PV MPPT performance under different temperatures

Fig. 7 PV MPPT performance of the proposed PEV system under different irradiances and temperatures

between 400 V and 600 V for various environmental conditions. Therefore, the maximum power point can be tracked directly without the help of an additional buck or boost converter.

In Fig. 7a, the irradiance level begins at 1000 W/m², decreases to 600 W/m², and subsequently increases to 800 W/m². At the start of the simulation, V_{pv} starts at 600 V and begins to track to V_{MPP}. After approximately 2 s, the maximum power point is reached and the PV array is producing 12.5 kW of active power to the system. After supplying 10 kW of active power to the battery, the excess power is feed into the grid as can be seen from the figures.

STATE GRID

STATE GRID ELECTRIC POWER RESEARCH INSTITUTE

Springer

At the irradiance level of 600 W/m², the lower maximum power point of approximately 7.5 kW is attained by the PV array. Therefore, the grid is required to top up an additional 2.5 kW of active power for PEV battery charging as shown in Fig. 7a. Meanwhile, at a irradiance level of 800 W/m², the maximum power point of approximately 10 kW is achieved by the PV array. Therefore, there is no net power transfer from the grid as the PV array is self-sufficient to meet the demand of the PEV battery.

In Fig. 7b, the operating temperature of the PV array starts at 25 °C, increases to 50 °C after 10 s and subsequently decreases to 35 °C. Similarly, it can be seen that the MPPT algorithm is able to track the maximum power with good proficiency. Since the PV array is producing power above the required power for PEV battery charging for all of the different testing temperatures, excess active power is transferred to the grid. Furthermore, the MPPT operation does not affect the reactive power transfer of the system as shown in the figures.

3.3 PEV charging performance

One of the most important aspects of the PEV charger is the ability to provide suitable charging profiles for PEV batteries depending on the battery's state of charge to ensure the safety of the person and vehicle as well as to preserve the battery's operating life. Examples of PEV battery types are a nickel metal hydride battery or lithium ion battery. The common charging profiles for PEV batteries are constant current, constant voltage and float charging. During constant current charging, the charging current is maintained at a specific level until the state of charge (SOC) of the battery reaches a certain level. Then, the charging profile is switched to constant voltage charging and the battery is charged at a constant voltage level while the charging current is decreasing. When the charging current reaches a certain level, the battery is fully charged and the battery voltage is maintained at a float voltage level. This profile is called float charging. Figure 8 illustrates that the charger with the proposed control strategy is able to provide all three charging profiles to the PEV battery with good dynamic and steady-state results.

3.4 System performance analysis

In order to comply with IEEE Standard 519, the grid current i_{abc} must have a THD less than 5% and its individual harmonic components must be well regulated. Figure 9 shows the harmonic spectrum of phase a current when the system is delivering 10 kvar of reactive power to the grid and 10 kW of active power to the battery. The system demonstrates a low THD count of 0.96% which is well within the regulation requirements of IEEE Standard
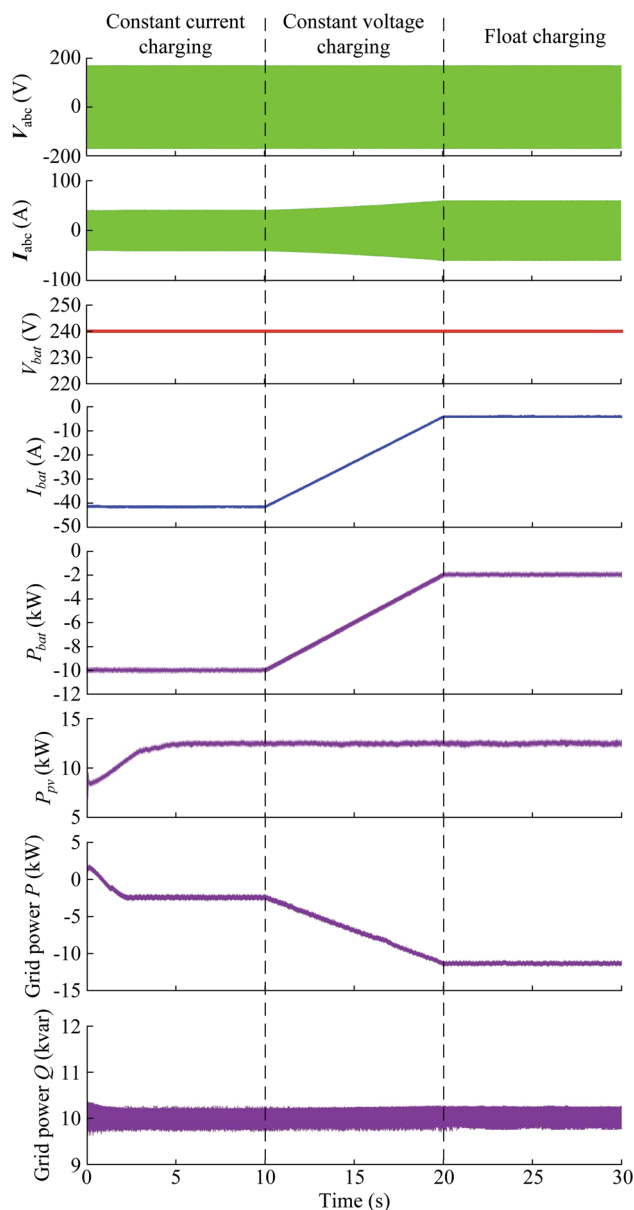

Fig. 8 PEV charger performance of the proposed PEV system for different battery charging profiles

519. The individual harmonic components of the phase current also show relatively low percentage of harmonic distortion throughout the spectrum.

Meanwhile, Fig. 10 shows the THD of the grid current phase a for various power flow modes under different power factors. From the figure, the four power flow modes represent the four quadrant operations of the PEV charger as depicted in Fig. 2. The power factor varying from zero to unity indicates that the PEV charger is supplying/receiving only reactive power initially while the reactive power decreases and active power increases gradually. As a result, the power factor increases until it reaches the value of one which indicates that the PEV charger is engaging in
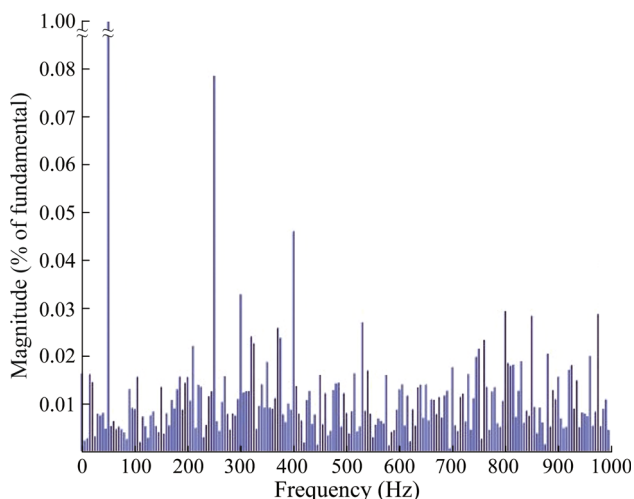
Fig. 9 Harmonic spectrum of phase a current with system parameters of $Q = 10$ kvar and $P_{bat} = -10$ kW (fundamental (50 Hz) is equal to 56.08, THD is equal to 0.96%)
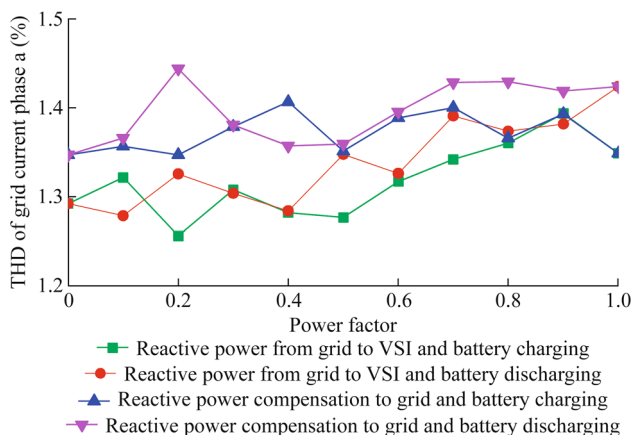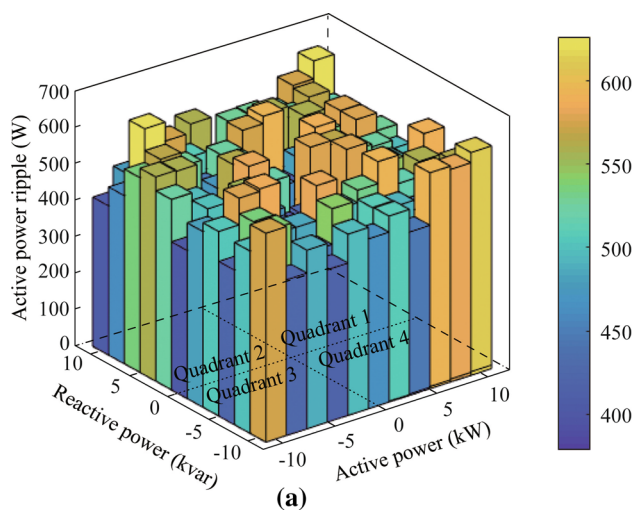

Fig. 10 THD of grid current phase a under various power factors for different modes of power flow

- Reactive power from grid to VSI and battery charging
- Reactive power from grid to VSI and battery discharging
- Reactive power compensation to grid and battery charging
- Reactive power compensation to grid and battery discharging

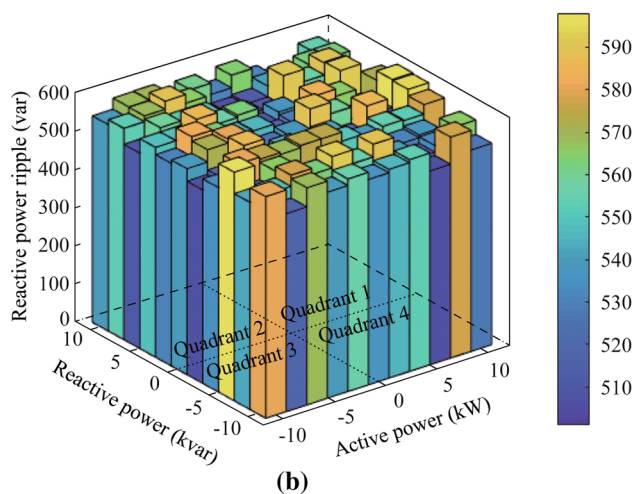**Fig. 11** Active and reactive power ripples for different quadrants

only the active power operation. As can be seen from Fig. 10, the system demonstrates low THD (less than 1.5%) in all four quadrants of operation.

In general, low active and reactive power ripple from the grid is desirable to minimize power loss due to oscillation as well as to produce balanced grid currents and voltages with low distortions. A study is conducted to evaluate the proposed system's active and reactive power performances. Figure 11 shows the active and reactive power ripples experienced by the system in different operating power quadrants.

From Fig. 11, we can see that the active power ripple experienced by the proposed charger increases with the magnitude of the net active power of the grid. However, the reactive power ripple of the system does not exhibit similar characteristics as that of the active power ripple and its

ripple fluctuates in a more random manner. Nevertheless, both active and reactive power ripples are relatively small, less than 700 W and 600 var respectively for maximum ripple experienced by the charger. Accordingly, the maximum active and reactive power ripple percentages are less than 7% and 8% respectively throughout all operating conditions, demonstrating the good performance of the charger and the MPC in place. Hence, power flow can be tracked with great accuracy as shown in the results before.

Another important aspect of the proposed system is the PEV charger performance characteristics. The charger's output voltage and current must be well regulated to protect and ensure the maximum operating life of the battery. A high charging current ripple could result in a temperature increase in the battery cells resulting in degradation of the battery. General limits for Li-ion and/or lead-acid batteries are RMS current ripples of 5%-10% of the rated charging
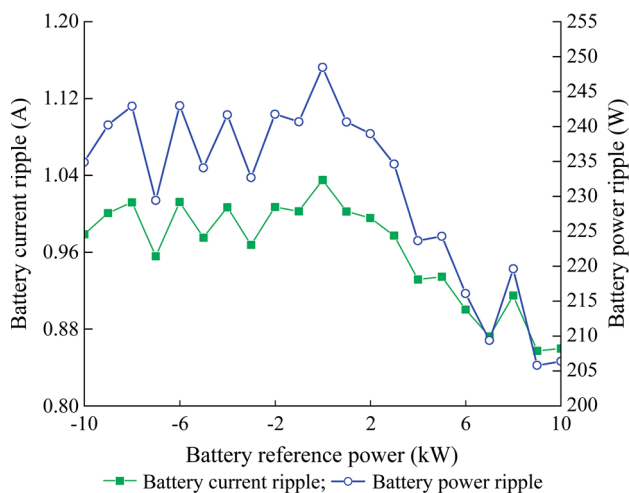
Fig. 12 Battery current and power ripples for various battery reference powers

current and RMS voltage ripples of 1.5% of the rated battery voltage.

Figure 12 shows the battery current and power ripples for various battery reference powers. Notably, the power ripple followed the current ripple as the battery voltage is set constant. During charging, it can be seen that the current ripple is lower for larger active power as compared to when the battery is delivering power to the grid. Overall, the charging current ripple is small (less than 1.04 A) and well within 5% of the rated charging current. As a matter of fact, the maximum percentage of current ripple per rated charging current experienced by the charger is about 2.5%. Furthermore, the battery power ripple is relatively low (less than 250 W) for the full range of battery reference power. Hence, the power loss due to oscillation is greatly minimized and the charger operates efficiently.

4 Conclusion

This paper presents a MPC of an off-board PEV charger with PV integration using two-level four-leg inverter topology. The control of the charger is realized by incorporating both direct power and current MPC that dynamically controls the decoupled real and reactive power flow as well as PEV battery charging and discharging current. The result shows that the charger using the proposed control strategy achieves four active-reactive quadrants of operations with PV integration with good steady-state and dynamic responses. PV power generation is seamlessly integrated into the charger while maximum PV power is consistently tracked for different environmental conditions. From the grid-side performance analysis, the charger

demonstrates less than 1.5% THD as well as low active and reactive power ripple of less than 7% and 8% respectively for all power flow modes.

Furthermore, the charger is able to provide good charging characteristics to the PEV battery for the different states of charge of the PEV battery as well as delivering a low charging and discharging current ripple of less than 2.5%. These results validate the performance of the proposed charger and its control strategy, hence the proposed charger is an excellent option for a PV integrated off-board charger in the charging stations.

Future research work on the proposed charger and its control can include: implementing long horizon predictive control to improve its control performance, a unified control algorithm for managing power flow to multiple PEV batteries concurrently, as well as charger topology improvements to further reduce THD, power ripples and charging ripples.

References

[1] Gunter SJ, Afridi KK, Perreault DJ (2013) Optimal design of grid-connected PEV charging systems with integrated distributed resources. IEEE Trans Smart Grid 4(2):956–967

[2] Yilmaz M, Krein PT (2013) Review of the impact of vehicle-to-grid technologies on distribution systems and utility interfaces. IEEE Trans Power Electron 28(12):5673–5689

[3] Veldman E, Verzijlbergh RA (2015) Distribution grid impacts of smart electric vehicle charging from different perspectives. IEEE Trans Smart Grid 6(1):333–342

[4] Heydt GT (1983) The impact of electric vehicle deployment on load management strategies. IEEE Power Eng Rev 2:41–42

[5] Luo A, Xu Q, Ma F et al (2016) Overview of power quality analysis and control technology for the smart grid. J Mod Power Syst Clean Energy 4(1):1–9

[6] Liu M, Mcnamara P, Shorten R et al (2015) Residential electrical vehicle charging strategies: the good, the bad and the ugly. J Mod Power Syst Clean Energy 3(2):190–202

[7] Kisacikoglu MC, Ozpineci B, Tolbert LM (2013) EV/PHEV bidirectional charger assessment for V2G reactive power operation. IEEE Trans Power Electron 28(12):5717–5727

[8] Izadkhast S, Garcia-Gonzalez P, Frias P (2015) An aggregate model of plug-in electric vehicles for primary frequency control. IEEE Trans Power Syst 30(3):1475–1482

[9] Falahi M, Chou HM, Ehsani M et al (2013) Potential power quality benefits of electric vehicles. IEEE Trans Sustain Energy 4(4):1016–1023

[10] Tanaka T, Sekiya T, Tanaka H et al (2013) Smart charger for electric vehicles with power-quality compensator on single-phase three-wire distribution feeders. IEEE Trans Ind Appl 49(6):2628–2635

[11] Pinto JG, Monteiro V, Gonçalves H et al (2014) Onboard reconfigurable battery charger for electric vehicles with traction-to-auxiliary mode. IEEE Trans Veh Technol 63(3):1104–1116

[12] Reddy KS, Panwar LK, Kumar R et al (2016) Distributed resource scheduling in smart grid with electric vehicle deployment using fireworks algorithm. J Mod Power Syst Clean Energy 4(2):188–199

[13] Chen C, Duan S (2015) Microgrid economic operation considering plug-in hybrid electric vehicles integration. J Mod Power Syst Clean Energy 3(2):221–231

[14] Yang Z, Li K, Niu Q et al (2014) A self-learning TLBO based dynamic economic/environmental dispatch considering multiple plug-in electric vehicle loads. J Mod Power Syst Clean Energy 2(4):298–307

[15] Kesler M, Kisacikoglu MC, Tolbert LM (2014) Vehicle-to-grid reactive power operation using plug-in electric vehicle bidirectional offboard charger. IEEE Trans Ind Electron 61(12):6778–6784

[16] Yilmaz M, Krein PT (2012) Review of battery charger topologies, charging power levels, and infrastructure for plug-in electric and hybrid vehicles. IEEE Trans Power Electron 28(5):2151–2169

[17] Kempton W, Letendre S (1997) Electric vehicles as a new power source for electric utilities. Transp Res 2(3):157–175

[18] Letendre SE, Kempton W (2002) The V2G concept: a new model for power? Public Util Fornightly 140(4):16–26

[19] Li X, Yao L, Hui D (2016) Optimal control and management of a large-scale battery energy storage system to mitigate fluctuation and intermittence of renewable generations. J Mod Power Syst Clean Energy 4(4):593–603

[20] Tang Z, Liu Y, Liu J et al (2016) Multi-stage sizing approach for development of utility-scale BESS considering dynamic growth of distributed photovoltaic connection. J Mod Power Syst Clean Energy 4(4):554–565

[21] Teng X, Gao Z, Zhang Y et al (2014) Key technologies and the implementation of wind, PV and storage co-generation monitoring system. J Mod Power Syst Clean Energy 2(2):104–113

[22] Brenna M, Dolara A, Foiadelli F et al (2014) Urban scale photovoltaic charging stations for electric vehicles. IEEE Trans Sustain Energy 5(4):1234–1241

[23] Liu N, Chen Q, Liu J et al (2015) A heuristic operation strategy for commercial building microgrids containing EVs and PV system. IEEE Trans Ind Electron 62(4):2560–2570

[24] Chen Q, Liu N, Hu C et al (2017) Autonomous energy management strategy for solid-state transformer to integrate PV-assisted EV charging station participating in ancillary service. IEEE Trans Ind Informatics 13(1):258–269

[25] Kisacikoglu MC, Kesler M, Tolbert LM (2015) Single-phase on-board bidirectional PEV charger for V2G reactive power operation. IEEE Trans Smart Grid 6(2):767–775

[26] Rivera S, Wu B, Kouro S et al (2015) Electric vehicle charging station using a neutral point clamped converter with bipolar DC bus. IEEE Trans Ind Electron 62(4):1999–2009

[27] Arancibia A, Strunz K, Mancilla-David F (2013) A unified single- and three-phase control for grid connected electric vehicles. IEEE Trans Smart Grid 4(4):1780–1790

[28] Bayhan S, Abu-Rub H (2014) Model predictive sensorless control of standalone doubly fed induction generator. In: Proceedings of 40th annual conference of the IEEE industrial electronics society, Dallas, USA, 29 October-1 November 2014, pp 2166–2172

[29] Petersson A, Harnefors L, Thiringer T (2005) Evaluation of current control methods for wind turbines using doubly-fed induction machines. IEEE Trans Power Electron 20(1):227–235

[30] Xu L, Zhi D, Williams BW (2009) Predictive current control of doubly fed induction generators. IEEE Trans Ind Electron 56(10):4143–4153

[31] Rodriguez J, Pontt J, Silva C et al (2007) Predictive current control of a voltage source inverter. IEEE Trans Ind Electron 54(1):495–503

[32] Cortés P, Kazmierkowski MP, Kennel RM et al (2008) Predictive control in power electronics and drives. IEEE Trans Ind Electron 55(12):4312–4324

[33] Cortes P, Wilson A, Kouro S et al (2010) Model predictive control of multilevel cascaded H-bridge inverters. IEEE Trans Ind Electron 57(8):2691–2699

[34] Panten N, Hoffmann N, Fuchs FW (2016) Finite control set model predictive current control for grid-connected voltage-source converters with LCL filters: a study based on different state feedbacks. IEEE Trans Power Electron 31(7):5189–5200

[35] Yaramasu V, Rivera M, Wu B et al (2013) Model predictive current control of two-level four-leg inverters—part I: concept, algorithm, and simulation analysis. IEEE Trans Power Electron 28(7):3459–3468

[36] Rivera M, Yaramasu V, Rodriguez J et al (2013) Model predictive current control of two-level four-leg inverters—part II: experimental implementation and validation. IEEE Trans Power Electron 28(7):3469–3478

[37] Young HA, Perez MA, Rodriguez J et al (2014) Assessing finite-control-set model predictive control: a comparison with a linear current controller in two-level voltage source inverters. IEEE Ind Electron Mag 8(1):44–52

[38] Mai R, Chen Y, Li Y et al (2017) Inductive power transfer for massive electric bicycles charging based on hybrid topology switching with a single inverter. IEEE Trans Power Electron 32(8):5897–5906

[39] Zhou D, Zhao J, Liu Y (2017) Finite-control-set model predictive control scheme of three-phase four-leg back-to-back converter-fed induction motor drive. IET Electr Power Appl 11(5):761–767

[40] Yaramasu V, Rivera M, Narimani M et al (2014) Model predictive approach for a simple and effective load voltage control of four-leg inverter with an output LC filter. IEEE Trans Ind Electron 61(10):5259–5270

[41] Chen Q, Luo X, Zhang L et al (2017) Model predictive control for three-phase four-leg grid-tied inverters. IEEE Access 5:2834–2841

Adrian Soon Theam TAN received B.S. and M.S. degrees in electrical engineering in 2014 and 2016, respectively, from Universiti Sains Malaysia (USM), Malaysia, where he is currently working toward the Ph.D. degree in electrical engineering. His current research interests include plug-in electric vehicle chargers, model predictive control for power electronics, and resonant power conversion.

Dahaman ISHAK received the B.Sc. degree in electrical engineering from Syracuse University, Syracuse, NY, USA, in 1990, the M.Sc. degree in electrical power from the University of Newcastle Upon Tyne, Newcastle upon Tyne, U.K., in 2001, and the Ph.D. degree from the University of Sheffield, Sheffield, U.K., in 2005. He was an electrical engineer with Goodyear Malaysia Berhad, Shah Alam, Malaysia, and was with Westport Malaysia Bhd, Port Klang, Malaysia. He is currently an associate professor with the School of Electrical and Electronic Engineering, Universiti Sains Malaysia,

Penang, Malaysia. His current research interests include high-performance permanent magnet brushless machines, electrical drives, and renewable energy.

Rosmiwati MOHD-MOKHTAR received her B.Eng. degree with honours and the M.Sc. in electrical and electronic engineering from Universiti Sains Malaysia in 1999 and 2002, respectively. She received her Ph.D. degree in electrical engineering from the Royal Melbourne Institute of Technology University, Australia in 2008. She joined the School of Electrical and Electronic Engineering, Universiti Sains Malaysia in October 2008 as a lecturer and researcher. Her research interests include system identification, advanced control system design, process modelling, process optimization, mechatronics applications and underwater system applications.

Sze Sing LEE received the B.Eng. (Hons.) and Ph.D. degrees in electrical engineering from the University of Science Malaysia,

Penang, Malaysia, in 2010 and 2013, respectively. He is currently an assistant professor in the University of Southampton Malaysia Campus, Johor Bahru, Malaysia. His research interests include alternative power converter topologies and their control strategies.

Nik Rumzi Nik IDRIS received the B.Eng. degree in electrical engineering from the University of Wollongong, Australia, the M.Sc. degree in power electronics from Bradford University, West Yorkshire, U.K., and the Ph.D. degree from Universiti Teknologi Malaysia (UTM) in 1989, 1993, and 2000, respectively. He is an associate professor at the Universiti Teknologi Malaysia, and currently the chair for the Power Electronics Chapter of IEEE Malaysia Section. His research interests include control of AC drive systems and DSP applications in power electronic systems.

STATE GRID
STATE GRID ELECTRIC POWER RESEARCH INSTITUTE